Variability of clouds and water vapor in low latitudes: View from Moderate Resolution Imaging Spectroradiometer (MODIS)

Philip W. Mote[1] and Richard Frey[2]

[1] This paper shows a small sampling of the atmospheric fields provided by the Moderate Resolution Imaging Spectroradiometer (MODIS), which is installed on both the Terra and Aqua satellites of the Earth Observing System. These fields include macroscale fields like cloud fraction, cloud top pressure, cloud optical depth, and column water vapor, and microscale fields like cloud particle effective radius. Most of the atmospheric fields resemble, in spatial pattern and temporal evolution, the cloud top temperature field; several, however, including effective radius and clear-sky water vapor, have markedly different spatial patterns and temporal evolution, suggesting that large-scale controls on tropical water vapor are more complicated than a simple connection with large-scale convergence and convection would suggest. As with several previous studies, the cloud top temperature or pressure has a bimodal distribution with peaks in both the lower and upper troposphere. Our analysis also reveals a dependence of cloud effective particle size on sea surface temperature.

1. Introduction

[2] A series of satellites launched by NASA and space agencies of other nations have provided an unprecedented view of the tropical atmosphere. The Terra satellite includes the Moderate Resolution Imaging Spectroradiometer (MODIS) whose 36 infrared and near-infrared channels provide richly detailed information about tropical clouds. The Aqua satellite includes a MODIS instrument and the Atmospheric Infrared Sounder (AIRS). It is now possible to combine and compare disparate types of measurements that either were not jointly available from the same platform or were not available at all.

[3] Clouds, water vapor, and sea surface temperature interact on a range of timescales in the tropics and subtropics, and generate important climate feedbacks. Phenomena of interest include the tropical intraseasonal oscillation, also known as the Madden-Julian Oscillation (MJO), and El Niño−Southern Oscillation (ENSO), both of which involve (in different ways) feedbacks between the ocean and atmosphere to produce variability at characteristic timescales that are determined internally as a product of complex dynamics rather than at a timescale of forcing (e.g., seasonal). Predictions of both MJO and ENSO offer the prospect of improving societal resilience to climate variations, and the

quality of predictions have improved considerably in recent years (see, e.g., *Wheeler and Hendon* [2004], for MJO).

[4] Feedbacks involving clouds, water vapor, radiation, and surface properties are of fundamental importance in determining global climate sensitivity (see *Stephens* [2005] for a cogent review). The intricate connections among these quantities make it difficult to construct simple feedback loops that accurately represent the real world; for example, it is clear [e.g., *Hartmann et al.*, 2001] that convection and cirrus do not conspire to produce an ''adaptive iris.'' Disentangling these intricate connections remains a challenging task both for observational and modeling studies, yet is crucial in understanding and predicting forced and unforced climate responses on a range of timescales.

[5] MODIS data offer the prospect of global coverage of a wide range of quantities on a wide range of timescales, at spatial resolutions down to 250 m, which can be used to address these and other questions. Some of the products on MODIS have not previously been available, and the combination of (1) a large number of fields available from the same instrument (2) a second MODIS flying a few hours behind the first, and (3) a range of other instruments on the same two platforms are all further advantages of MODIS. In this paper a few of the quantities and the joint relationships among them are examined. A few intriguing features are highlighted for further inquiry.

2. MODIS Data

[6] Launched on 18 December 1999, Terra is a Sun-synchronous polar orbiting satellite at 705 km altitude that crosses the equator southward (descending) at 1030 LT and

[1]NorthWest Research Associates, Bellevue, Washington, USA.
[2]Space Science and Engineering Center, University of Wisconsin-Madison, Madison, Wisconsin, USA.

again northward (ascending) at 2230 LT. Terra MODIS began collecting data in late February 2000 [*Barnes et al.*, 1998]. Aqua was launched 4 May 2002 and is in a similar orbit but with crossing times at 0130 and 1330 LT. Aqua is the lead satellite in the so-called A-train, a string of six satellites flying in a line a few minutes apart [*Stephens et al.*, 2002]. For this study we focus on data from Terra, mentioning Aqua only because another MODIS data set is available.

[7] MODIS has 36 spectral bands from 0.415 to 14.235 μm; of these, 26 bands are used for atmospheric sensing [*Barnes et al.*, 1998]. Cloud products include cloud top pressure, cloud top temperature (derived from cloud top pressure using a suitable temperature profile), and effective emissivity, all from the 11 μm and CO_2 bands (31–36); and cloud optical thickness, particle effective radius, and water path, from bands in the visible, near infrared, shortwave infrared and medium wave infrared (bands 1, 2, 5, 6, 7, and 20) [*Platnick et al.*, 2003].

[8] The method used to derive cloud top pressure, CO_2 slicing, is applied at altitudes above about the 700 hPa level [*Platnick et al.*, 2003]. Three of the four CO_2 bands on MODIS are either weakly sensitive or insensitive to clouds whose tops are lower than the 700 hPa level; therefore, for low clouds, the cloud top pressure is derived solely from the 11 μm band assuming that the cloud is optically thick.

[9] Although it is a nadir-viewing instrument, MODIS provides retrievals of atmospheric profiles of temperature, ozone, and water vapor (summed to produce total precipitable water). These profiles are derived using radiances from 12 infrared bands and regression coefficients derived from 8400 radiosonde profiles [*King et al.*, 2003; *Seeman et al.*, 2003].

[10] In order to enable large-scale studies such as this one, the retrieved quantities (Level 2), which have a resolution ranging from 250m to 5km, are assembled into $1° \times 1°$ bins on a regular latitude-longitude grid (Level 3, or L3). Various statistics summarize the variability of the thousands of pixels that comprise a single L3 bin: mean, minimum, maximum, and standard deviation, and often quality-weighted versions of the same statistics. Level 3 data are available as daily, 8-day, and monthly products. Some fields (e.g., water vapor-near IR) require reflected sunlight and hence are derived only in daytime; others (e.g., cloud top pressure) are derived for both day and night, and are available both separately and combined.

[11] This analysis uses the current version of MODIS data, known as collection 4. At the time of writing, reprocessing of the data for collection 5 had recently begun and is expected to be completed by 2007. We note below where collection 5 is expected to differ from the results shown here. Both daily and monthly data L3 are used. We use daily data for the period 1 November 2002 through 28 February 2003, a time period chosen because it included a moderate El Niño event and moderately strong MJO activity, which are explored in a subsequent paper. Because this period is somewhat unusual, the question arises as to whether the analyses shown here are representative of other time periods. The sheer size of the daily files (400 Mb/d) precluded extensive analysis of daily data at the time this analysis began, but since then the data distribution center has introduced a subsetting feature that substantially reduces

file size, and the analysis has been repeated in limited fashion for the period June through August 2003.

## 3. Mean Fields

3.1. Monthly Mean Maps

[12] We begin by showing, for December 2002, the sea surface temperature (SST) from the Reynolds optimal interpolation [*Reynolds et al.*, 2002] followed by a small sampling of some key atmospheric fields provided by MODIS (Figure 1). December 2002 fell during a moderate El Niño event, which shifted the highest SSTs and most active convection eastward toward the dateline. SSTs (Figure 1a) exceeded 29°C over much of the western and central Pacific, as is typical during El Niño events.

[13] The MODIS fields shown (Figures 1b–1j) are monthly means of daily L3 data. Averaged day and night cloud top pressure (Figure 1b) and temperature (not shown, the correlation with pressure is 0.92, and 0.98 in the tropics) show regions of high, cold clouds and regions of warm, low clouds. Regions of high, cold clouds are mostly associated with tropical deep convection over tropical land areas in South America, Indonesia, and central Africa, and over the Indian Ocean, the western Pacific (shifted eastward during this El Niño year) and South Pacific Convergence zone. Some high, cold clouds appear also over the Tibetan Plateau [*Gao et al.*, 2003]. Warm, low clouds predominate over the subtropical oceans and over the eastern Pacific, where atmospheric subsidence suppresses convection. In most of these subtropical regions cloud fraction (to be shown below) is low, and when clouds do occur their tops are typically 10°C or warmer, and at pressures of 800 hPa or higher.

[14] Terra and Aqua each make two passes per day, permitting a crude estimate of the diurnal cycle in cloud top pressure (Figure 1d). Over most land areas, nighttime (roughly 2230LT) pressures are lower by about 100 hPa, and over northern Australia the differences exceed 300 hPa. Largest differences occur where daily averaged cloud top pressure is low (not shown), indicating a very large altitude range in cloud top associated with convective cloud. Geostationary satellites indicate that the phasing of the diurnal cycle in 11 μm brightness temperature, which approximates cloud top temperature, depends on surface type (land or ocean) and on cloud top temperature itself: land areas have a much larger diurnal cycle with a peak (highest temperature, lowest cloud top altitude) around midnight LT and the peak cloud amount occurs somewhat earlier for higher colder clouds [*Tian et al.*, 2004]. The 2230 LT overpass of Terra catches land-based convection near its peak but is ill-timed for estimating the smaller diurnal cycle over oceans.

[15] Straddling the west coast of Africa at about 10°N is a small region covering both ocean and land areas, with fairly large negative difference in day-night cloud top pressure (i.e., 1030 LT pressure lower than 2230 LT). This area was the focus of studies of the diurnal cycle in clouds from early satellite measurements [*McGarry and Reed*, 1978] which revealed a diurnal cycle in convective cloud fraction with maximum between 2100 LT and 0300 LT over land and between 1200 and 1800 LT over oceans.

[16] Most of the fields are highly correlated with cloud top pressure, owing to the fundamental difference between convective and nonconvective regions. These include sev-
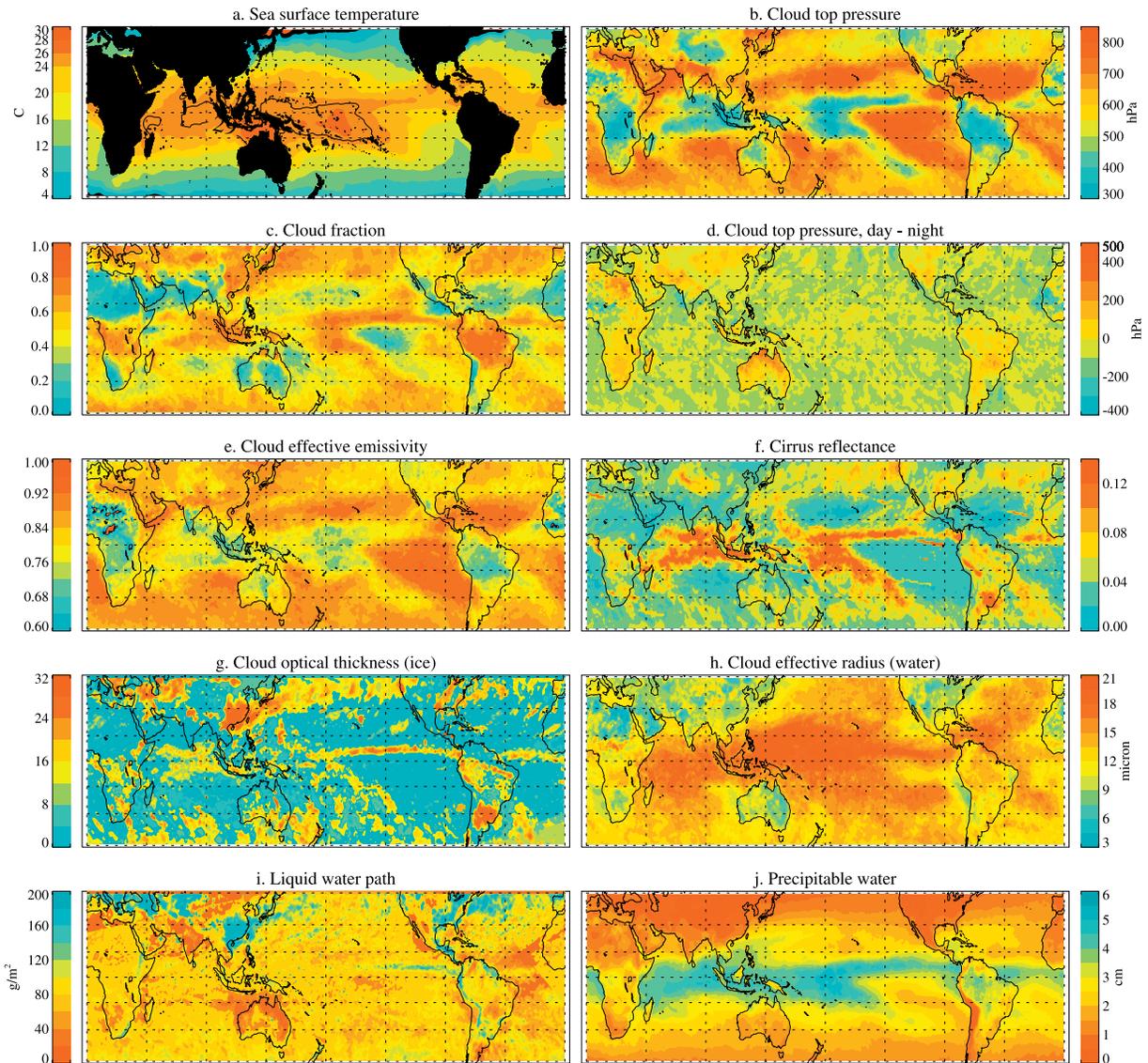
Figure 1. Maps of MODIS Terra level 3 data for December 2002, for the fields indicated in Figures 1b–1l. The SST data (Figure 1a) come from the NOAA optimal interpolation 1° × 1° data set [*Reynolds et al.*, 2002], and the black curve indicates the 29°C isotherm. See text for definition and derivation of the various quantities shown.

eral of the fields shown, as well as high cloud fraction, minimum and maximum values and standard deviations of cloud top temperature and pressure for both day and night. We have chosen here to highlight several fields whose distributions are fairly different from cloud top pressure, as well as physically significant and interesting.

[17] There are several cloud fraction products, of which one is presented here (Figure 1c). The L2 cloud mask (in the MOD35 processing stream) uses several groups of tests, employing up to 20 of the 36 MODIS channels, to determine the likelihood that a 1-km pixel is cloudy; there are four levels of confidence in the results of the cloud mask, including "cloudy" and "probably cloudy" [*Platnick et al.*, 2003]. The L3 1° ×1° "cloud fraction infrared" product is simply the aggregation of the L2 counts of "cloudy" and "probably cloudy" [*Platnick et al.*, 2003]. The "cloud fraction total" (Figure 1c) field is derived through a

completely different process, as part of the cloud microphysics package, which also determines the phase of cloud particles (liquid, solid, or mixed/uncertain); "total" refers to all phases of water [*Platnick et al.*, 2003].

[18] The two cloud fraction fields are highly correlated with each other (0.89 between 45°S and 45°N) but the means are significantly different, 0.61 for "cloud fraction total" and 0.70 for "cloud fraction infrared". The difference between fields is largest over oceans. (This difference occurs because the MOD35 ("cloud fraction infrared") cloud mask has too much cloud over oceans at night, producing a high bias in cloud fraction infrared. This will change in collection 5.) Both fields are anticorrelated with cloud top temperature and pressure, meaning locations with high likelihood of cloudiness also experience frequent deep convection. Two important exceptions are the subtropical eastern parts of the southern Atlantic and southern Pacific

basins, where persistent stratocumulus shows up in Figure 1c as large values of cloud fraction and in Figure 1b with high cloud top pressure (low cloud top height). Another exception is in western Australia where mean cloud top pressure and temperature are low, high cloud fraction (not shown) is fairly high relative to the mean for that field, but total cloud fraction is relatively low.

[19] Cloud effective emissivity (Figure 1e) is defined as cloud fraction times cloud emissivity, and is retrieved simultaneously with cloud top pressure using the CO_2 slicing technique at pressures (<700 hPa) where CO_2 slicing is performed [*Platnick et al.*, 2003]. Since the CO_2 slicing technique is applied only at pressures below 700 hPa, a different approach must be used for lower clouds; at present, for low clouds the cloud fraction and cloud emissivity are both assumed to be unity, which leads to frequent values of unity for cloud effective emissivities in regions of low cloud. Even including the convective regions, the most common value of cloud effective emissivity in the tropics is unity, eclipsing the second mode in the frequency distribution (around 0.8) by a factor of ten. In the next version of MODIS data, collection 5, cloud effective emissivities will be set equal to cloud fraction, which will substantially reduce the prevalence of high values in the subtropics. The distribution of cloud effective emissivity is similar to that for cloud fraction (Figure 1c) from which it is derived.

[20] Cirrus reflectance (Figure 1f) is defined as reflectance of sunlight (hence only available during daytime) at 1.38 μm, a wavelength that is strongly attenuated by water vapor and hence can only be used to detect clouds at high altitude. The retrieval uses 1.38 and 0.66 μm reflectances together in order to account for absorption of water vapor above the cirrus cloud [*Gao et al.*, 2002]. Values of cirrus reflectance are strongly skewed, with a mode near zero and a long tail to higher values. The field is near zero in the regions where low clouds predominate and near 0.1 elsewhere. Its spatial pattern resembles those of most other cloud fields (Figures 1b, 1c, and 1e) but with much sharper distinctions between low and high values (see, e.g., the ITCZ in the central and eastern Pacific). One value of the cirrus reflectance field is for removing the effects of cirrus from surface fields [*Gao et al.*, 2002], which evidently are minimal in most of the subtropics. In a study of satellite data with high temporal resolution, *Soden* [2004] showed that the moistening of the upper troposphere occurs as cirrus is forming, not dissipating, suggesting that cirrus itself is not the dominant source of upper tropospheric moisture but rather both are caused by the same mesoscale circulation.

[21] Cloud optical thickness of ice clouds (Figure 1g) is quite different from the other fields shown. Many of the features have smaller spatial scale, especially the narrow intertropical convergence zone in the Pacific Ocean, where optical thickness is quite high. Ice clouds in the midlatitude storm tracks also have high optical thickness. Ice water path (not shown) has spatial patterns very similar to optical thickness for ice clouds, even more similar than would be expected based on the study of *Heymsfield et al.* [2003]. The patches of high optical thickness over eastern China and subtropical South America are fairly persistent features, showing up in most months (less commonly in April-September) and in the long-term mean. They are probably

not artifacts of the retrieval, as their shape and location changes and they disappear entirely in some months. The climatological conditions giving rise to these features are beyond the scope of this paper.

[22] Cloud optical thickness for water clouds (not shown) has remarkably uniform values (<6) throughout the tropics over water, with slightly higher values appearing over some land areas and the same patches of high optical thickness over eastern China and eastern North America as were seen in the ice cloud optical thickness field, but not the one over subtropical south America. In other months this feature does appear in the water cloud optical thickness field.

[23] Cirrus reflectance and cloud optical thickness have more sharply defined features, especially in the ITCZ, than most of the other fields shown here. By contrast, the spatial scales in cloud effective radius (Figure 1h) are considerably greater than for the other fields. Cloud effective radius is large over most tropical ocean areas and smaller over continents, especially in the northern hemisphere. This retrieval is done in conjunction with that for cloud optical thickness, using six bands in the visible and near infrared as discussed by *Platnick et al.* [2003] and represents the effective radius and optical thickness of the entire cloud because the different wavelengths are absorbed to different degrees. The spatial variability of this field can be understood in part from the surface type and temperature and its connection with convective activity. *Sherwood* [2002], using the 3.7 μm channel of AVHRR, found that effective radius was typically 10–20% lower over land than over ocean, most likely owing to the availability of aerosols as cloud condensation nuclei. Effective radius may depend on the strength of convective updrafts; this is a point to which we return below.

[24] Liquid water path (Figure 1i) closely resembles the field of optical thickness for water clouds (not shown), and the water path for ice (not shown) resembles the optical thickness for ice clouds (Figure 1g). The fine-scale line of the ITCZ which shows up so clearly in the optical thickness for ice clouds is confined to the eastern Pacific with liquid clouds. Perhaps this is because the ITCZ is more narrowly confined there owing to the sharper north-south gradients of SST.

[25] Column (or precipitable) water vapor is retrieved using two different methods, IR and near-IR. In the IR method, profiles of water vapor are derived using regression of infrared channels as discussed in section 2, and these profiles are summed vertically to give a column value. The near-IR method uses five channels near 0.94 μm, measuring attenuation of solar near-IR above reflective surfaces like clouds, land, and sunglint regions of the oceans [*Gao and Kaufman*, 2003]. The restriction to reflective surfaces means that retrievals for clear pixels at low solar zenith angles, as is the case for middle latitudes in winter, are not attempted, and there are other problems with both the above-cloud and clear-sky near-IR water vapor, especially over the oceans (e.g., dependence on zenith angle and inconsistency with cloud top height).

[26] The precipitable water field q_{clr} (Figure 1j) more closely resembles SST over oceans than it resembles the various cloud fields (Figures 1b–1i). Over land, the dry area over South America west of the Andes is also relatively cloud-free (Figure 1c) and also appears very dry in the near-
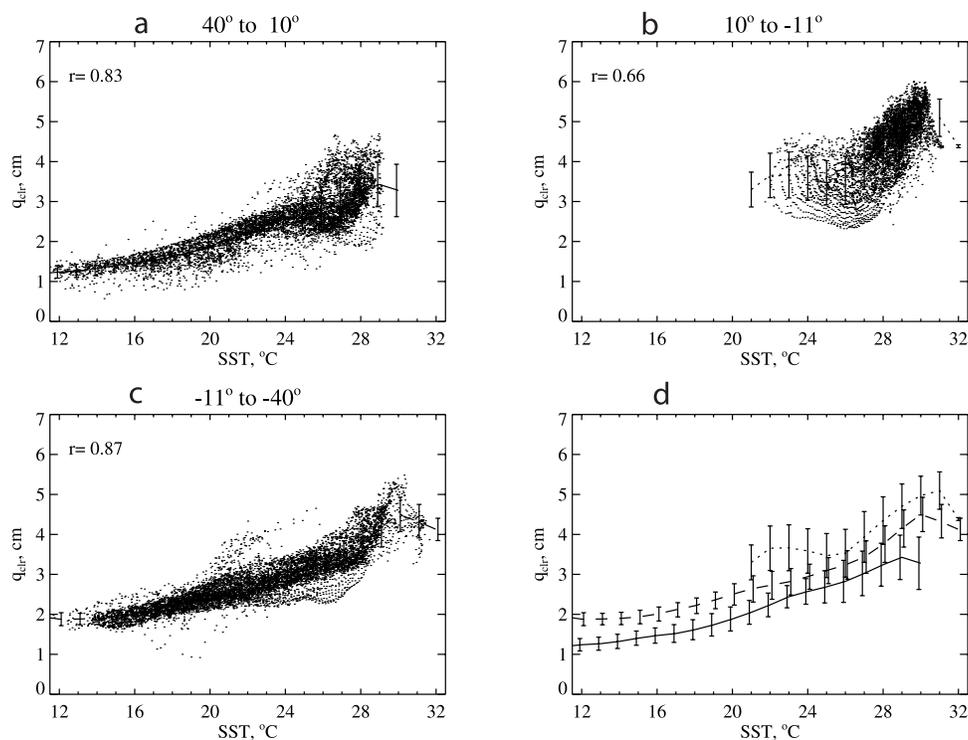
Figure 2. Scatterplot of mean clear-sky water vapor against SST in December 2002 for 1°C bins, for three latitude zones objectively determined (see text for details). Figure 2d shows the mean and ±1 σ for all three zones.

IR clear-sky water vapor field (not shown) but has no counterpart in other fields. The IR water vapor is sometimes too high over land, especially over desert areas, but that further emphasizes that these low values west of the Andes are likely real.

[27] Bearing in mind that this retrieval is performed only for clear pixels, these results underscore that even in clear areas near convection, column water vapor is generally much higher than in nonconvective regions, but also that there is not always a close correspondence between cloud and water vapor.

[28] Of critical interest is the relationship between SST and q_{clr}, because of the role of water vapor as a greenhouse gas, and the climatic feedbacks associated with these two quantities on all timescales. Figure 2 shows scatterplots of these two quantities for different latitude zones, with the boundaries between latitude zones selected objectively to minimize the sum of squared errors from binning q_{clr} against SST in 1°C bins. Different relationships obtain in the northern subtropics (40°N−10°N), tropics (10°N−11°S), and southern subtropics (11°S−40°S). In both northern and southern subtropics, there is a strong positive correlation between q_{clr} and SST. In the tropics, though, there is not a simple relationship between SST and q_{clr}. For SST between 20° and 25°C, found west of South America and in the Gulf of Guinea west of Africa, mean q_{clr} declines slightly with increasing SST, whereas above 25°C mean q_{clr} increases. (For narrower latitude bins these relationships are even clearer.) *Frey et al.* [1996], using HIRS and AVHRR data, showed that the spectral greenhouse parameter in wavelengths dominated by middle tropospheric water vapor are broadly correlated with sea surface temperature but also

that this relationship becomes more complicated at higher SST. Our findings extend their work and demonstrate the geographic dependence of this relationship.

[29] We have repeated this analysis for each of the months June, July, and August 2003, and although the dividing latitudes are farther north, the basic relationships (not shown) are the same, with a couple of interesting exceptions. First, the gap in the subtropical curves is substantially narrowed, because the northern subtropical curve moved up and mostly lines up with the southern subtropical curve. Second, for SST values greater than 30°C in the northern subtropics, the mean water vapor gets very low (less than 2 cm) because these points are all in the Red Sea and Persian Gulf, where very high SST occurs below clear, dry subsiding air.

[30] These results stand in contrast to those expected from modeling studies [*Larson and Hartmann*, 2003a, 2003b] that suggest monotonic increases in atmospheric water vapor with SST, at least for "aqua-planet" lower boundary conditions, for zonally uniform or zonally varying SST. As noted by, for example, *Lau et al.* [1996], the relationship between SST and water vapor or the water vapor greenhouse effect is controlled on very large scales by atmospheric circulation, rather than by local thermodynamics.

3.2. Bimodality of Cloud Top Height

[31] Univariate PDFs of cloud top pressure have a bimodal distribution with a sharp mode for low clouds at a temperature of about 290K and a pressure of 900 hPa, and a long tail with a second mode at a pressure of about 230 hPa (Figure 3a). When binned against cloud top temperature for equal-size bins (not shown), the upper tropospheric mode
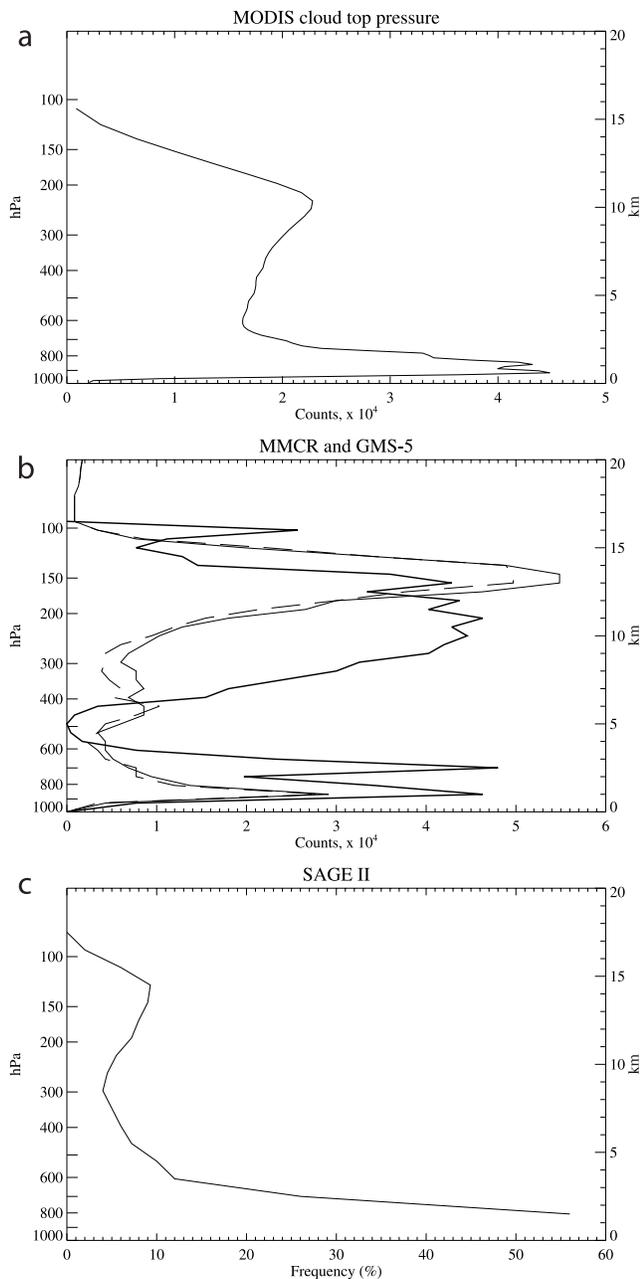
Figure 3. Histograms of cloud top height or pressure from (a) MODIS, 15°S–15°N, November 2002 through February 2003 at 1° × 1° resolution; (b) millimeter wave cloud radar at Manus Island, August 1999 through October 2000, for day (thin solid) and night (dashed); and GMS-5 daytime satellite observations near Manus for the same time period (thick; multiplied by 200 for comparison) [from *Hollars et al.*, 2004]; and (c) SAGE II, 20°S–20°N, 1986 [from *Wang et al.*, 1995].

flattens substantially. We find no evidence, in either the cloud top temperature or cloud top pressure distribution, for a third mode like that identified by *Johnson et al.* [1998] associated with detrainment of cumulus congestus near the freezing level.

[32] Bimodality in cloud top height has been observed in several other data sets, summarized in Figures 3b and 3c.

Hollars et al. [2004] (Figure 3b) compared data from ground-based radar (MMCR) in the western Pacific with coincident data from GMS-5, which is a satellite platform using nadir viewing at 0.65 and 11 μm wavelengths. The coincident GMS-5 retrievals in daytime had an upper mode that was shifted too low in altitude, and had no upper mode in the nighttime retrievals presumably owing to the use of a visible wavelength (0.65 μm) in the retrieval (this issue was not discussed by *Hollars et al.* [2004]); the radar data showed little day-night difference. The radar data at Manus also suggest a third mode near 6km, possibly associated with the freezing level as suggested by *Johnson et al.* [1998]. Retrievals from SAGE II (Figure 3c) [*Wang et al.*, 1995], a satellite platform using limb-viewing occultation of solar radiation, also show bimodality. However, bimodality was not observed in HIRS data, from a satellite platform using nadir viewing with several channels between 13 and 15 μm [*Wylie and Wang*, 1997].

[33] In these studies, the seasons, locations, and altitudes of maximum upper level cloud fraction varied considerably; the MODIS data, however, compare far better with the radar data than did the GMS-5 satellite data [*Hollars et al.*, 2004]. Without carefully screening the data for maximum comparability, Figure 3 cannot be considered an instrument intercomparison, merely a demonstration of the prevalence of bimodal distributions of cloud top height, pressure, or temperature in the tropics.

3.3. Relationships Among Fields

[34] Relationships among these fields are illustrated in scatterplots and in joint, or bivariate, probability density functions (PDFs). These PDFs are a good way to identify nonlinear relationships between variables, in contrast to linear techniques like correlation analysis. We construct them using daily 1° × 1° fields from 1 November 2002 through 28 February 2003, between 15° S and 15° N. This 4-month time period was chosen partly because daily-timescale studies are challenging with data volumes this large (400 Mb/d), and partly because this was a particularly interesting time period with a moderate El Niño event and fairly vigorous intraseasonal variations associated with the Madden-Julian Oscillation. As a check of the representativeness of these results, the period 1 June 2003 through 31 August 2003 was also examined, offering a contrast in seasonal, intraseasonal and interannual variability. The joint PDFs were substantially similar to those for the 1 November 2002 to 28 February 2003 period.

[35] There is a strong relationship between cloud top temperature and optical thickness for most clouds (Figure 4a). Previous studies of this subject (e.g., *Hartmann et al.* [2001] with ISCCP data) used far fewer (1% as many) bins for the joint PDF and although these results are consistent with the ISCCP data, they also reveal additional features. The vast majority of clouds have optical thickness $\tau < 10$, though the population of optical thicknesses spreads out considerably for cloud top temperatures less than about 215K with thick clouds being almost as likely as thin clouds. Slicing the joint PDF the other way, clouds with large optical thickness are likely to have cold, high cloud tops. However, the converse is not true: clouds with cold, high tops are about as likely to be optically thin as optically thick.
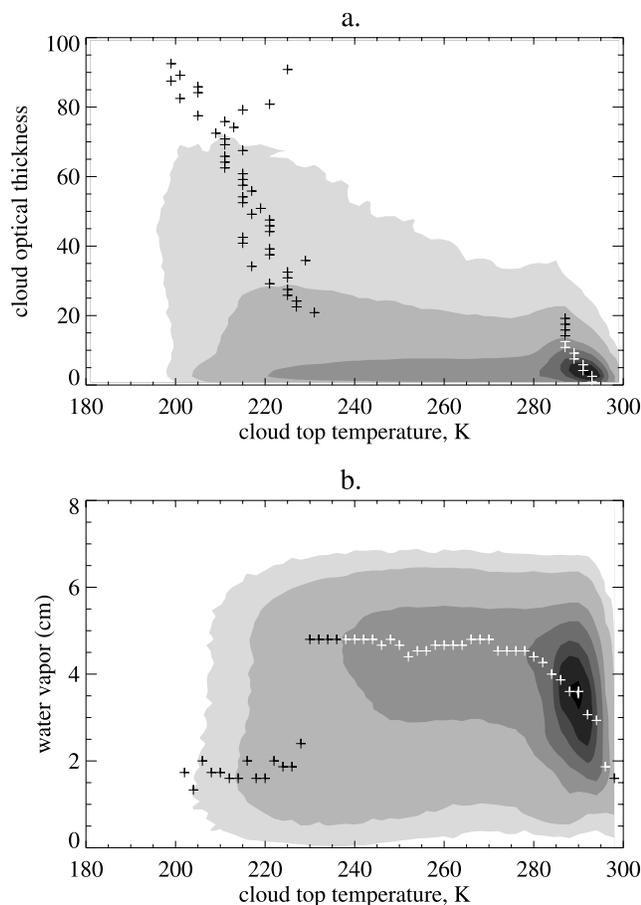
Figure 4. Joint probability distribution functions for the pairs of variables indicated, summed over the 45°S–45°N domain for daily values for November 2002 through February 2003. For each variable there are 60 bins. Pluses show the mode of the distribution of the variable on the abscissa, for each bin of the variable on the ordinate. Contours enclose 0.1, 1, 10, 25, 50, 70, 95, and 99% of the data.

[36] Water vapor derived from the IR channels shows an interesting relationship with cloud top temperature (Figure 4b). Recall that what is shown is an aggregation of pixel-level results within 1° × 1° grid boxes; cloudy pixels register a cloud top temperature and clear pixels register a water vapor value, so what is shown is the association of the two fields in close proximity but not at exactly the same location. For high cloud top temperatures (>280 K), the mean and modal water vapor decline owing to the fact that these locations (e.g., west of South America) experience subsiding dry air above stratocumulus clouds, so that a dry column overlies shallow persistent clouds. For clouds with tops in the middle troposphere (which are less common; see Figure 3), there is a fairly constant shape of the PDF of water vapor (with a mode at about 4.5 cm) for a wide range of cloud top temperatures; that is, the meteorological conditions in which such clouds are found support the same broadly distributed water vapor PDF regardless of cloud top height. In the upper troposphere (<240 K), a weakly bimodal distribution of water vapor develops, with both very dry (mode around 2 cm) and more typical (4.5 cm)

column water vapor amounts. This may be related to the bimodal distributions of upper tropospheric water vapor noted by *Brown and Zhang* [1997] and *Zhang et al.* [2003] although the values presented here are column values whereas they found bimodality only in the upper troposphere. A similar bimodality appears in the near-IR water vapor product above clouds (not shown), but when compared with colocated cloud top pressure the column water vapor is much too high in the upper troposphere. This discrepancy may be related to saturation in the 1.24 μm channel above bright tropical clouds, a problem which will be fixed in collection 5 (B. Gao and R. Hucek, personal communication, 2006).

[37] Water vapor for clear pixels derived from the near-IR channels, on the other hand (not shown), has a near-Gaussian distribution with a mean and mode near 3.5 cm, and shows no relationship with other variables in joint PDFs. This may be related to the problems, previously noted, that this product has over oceans.
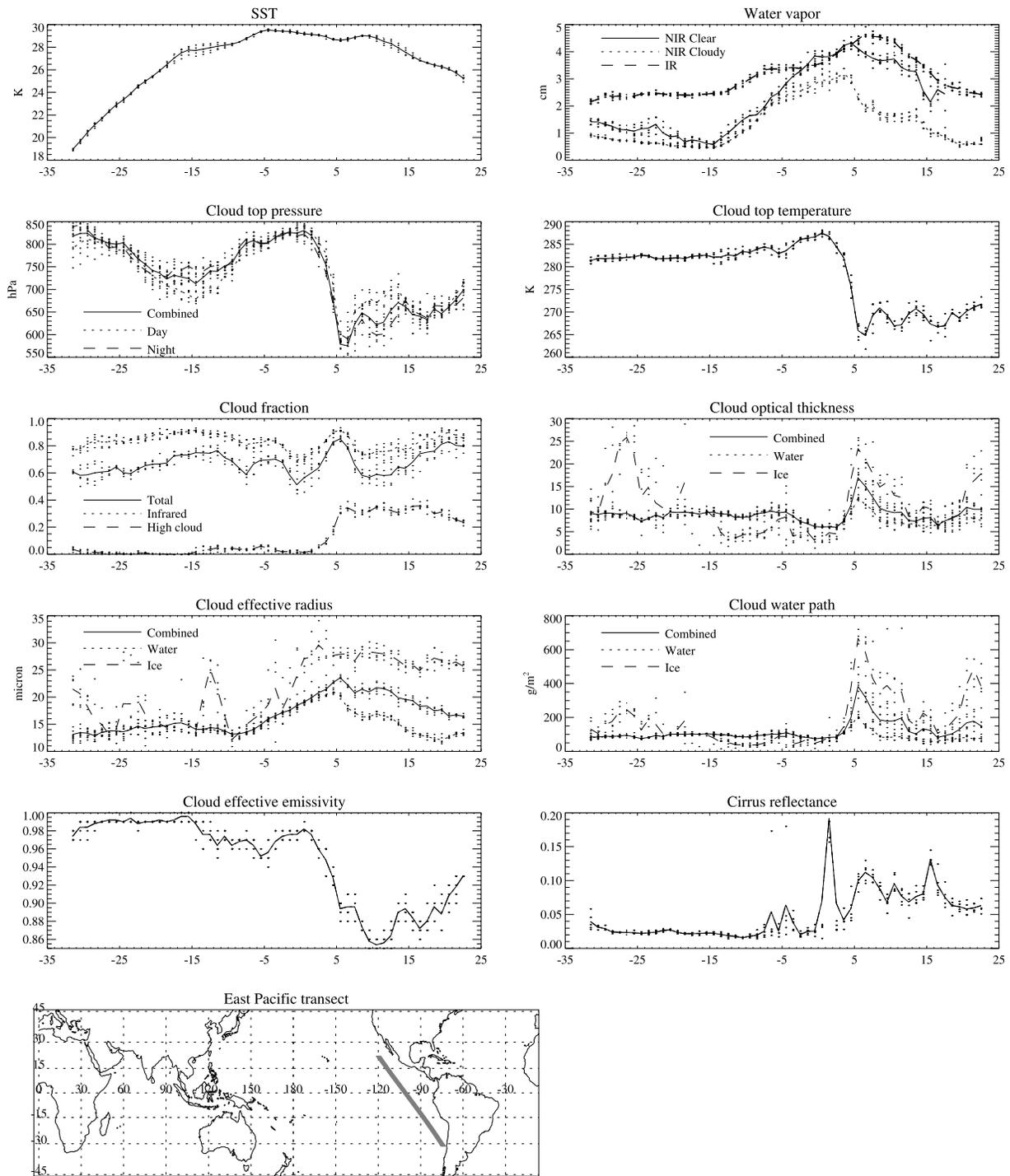
3.4. Transects

[38] Relationships among fields show interesting variability along transects. The first transect (Figure 5) extends from the northern to the southern subtropics in the eastern Pacific, across the slender ITCZ at about 5°N. Although all three areas have fairly uniformly large cloud fraction (0.6–0.8), in most respects they have substantially different properties. In the ITCZ, cloud fraction is slightly higher, and cloud optical thickness and cloud water path have a sharp peak at 5°N.

[39] The northern subtropics and nonconvective tropics share many properties with the ITCZ. In and north of the ITCZ, cloud top temperatures are below freezing, so ice clouds are observed, raising the cloud effective radius, cloud optical thickness, and cloud water path, and lowering the cloud effective emissivity. Cirrus clouds are also occasionally observed, so the cirrus reflectance is higher (the spike at 1.5° N seems to be spurious) and the high cloud fraction (i.e., frequency of observations with cloud top pressure <400 hPa) is relatively high. There is a substantial difference between IR precipitable water and near-IR clear-sky water vapor, and also between near-IR clear-sky and above-cloud water vapor.

[40] South of the equator, properties are quite different from those at the same SST in the northern subtropics. In a region from 10°S–25°S, cloud top temperature is nearly constant at about 282 K but cloud top pressure varies from 800 to 700 hPa and has a fairly large diurnal cycle for a marine area. Cloud effective radius is uniform and small, and high cloud fraction is approximately zero. Column water vapor is substantially lower than it is north of the ITCZ, though this contrast is much smaller in the IR water vapor product than in the near-IR product.

[41] Along the ITCZ (Figure 6), defined for each longitude except near and over Africa as the 5°-wide band centered on the latitude of minimum cloud top pressure, variations in most quantities (except SST) are substantially greater than along the tropical portion of the East Pacific transect. Linear correlations are summarized in Table 1 but in many cases the relationships are not linear.

[42] Some noteworthy features of this transect include (1) three areas of low cloud top pressure evident in Figure 1b

Figure 5. Variation of quantities shown along a 5°-wide transect in the eastern Pacific (see map at bottom left) for December 2002. In each panel, the mean of the 5° transect is plotted as a curve and the individual grid point values (5 per latitude) are shown as dots. Abscissa is latitude.

(Indian Ocean, central Pacific, and South America) are also areas where cloud fraction exceeds 0.8 or even 0.9; (2) strong negative correlations between cloud top pressure and cloud fraction, and strong positive correlations between cloud top pressure and cloud effective emissivity; (3) cirrus reflectance is highest at or, in the Indian Ocean, a bit west of the lowest cloud top pressure (4) cloud optical depth and cloud water path have the largest variability at short spatial scales.

[43] Although in some instances the relationships between fields in the ITCZ as well as elsewhere are linear (e.g., cloud top pressure and effective emissivity, r = 0.76), in other instances they show interesting nonlinear relationships. Sometimes the relationships are distinct from those outside the ITCZ. Cloud particle effective radius shows a relationship between SST for both water clouds and ice clouds (Figure 7). Ice cloud particle effective radii are larger
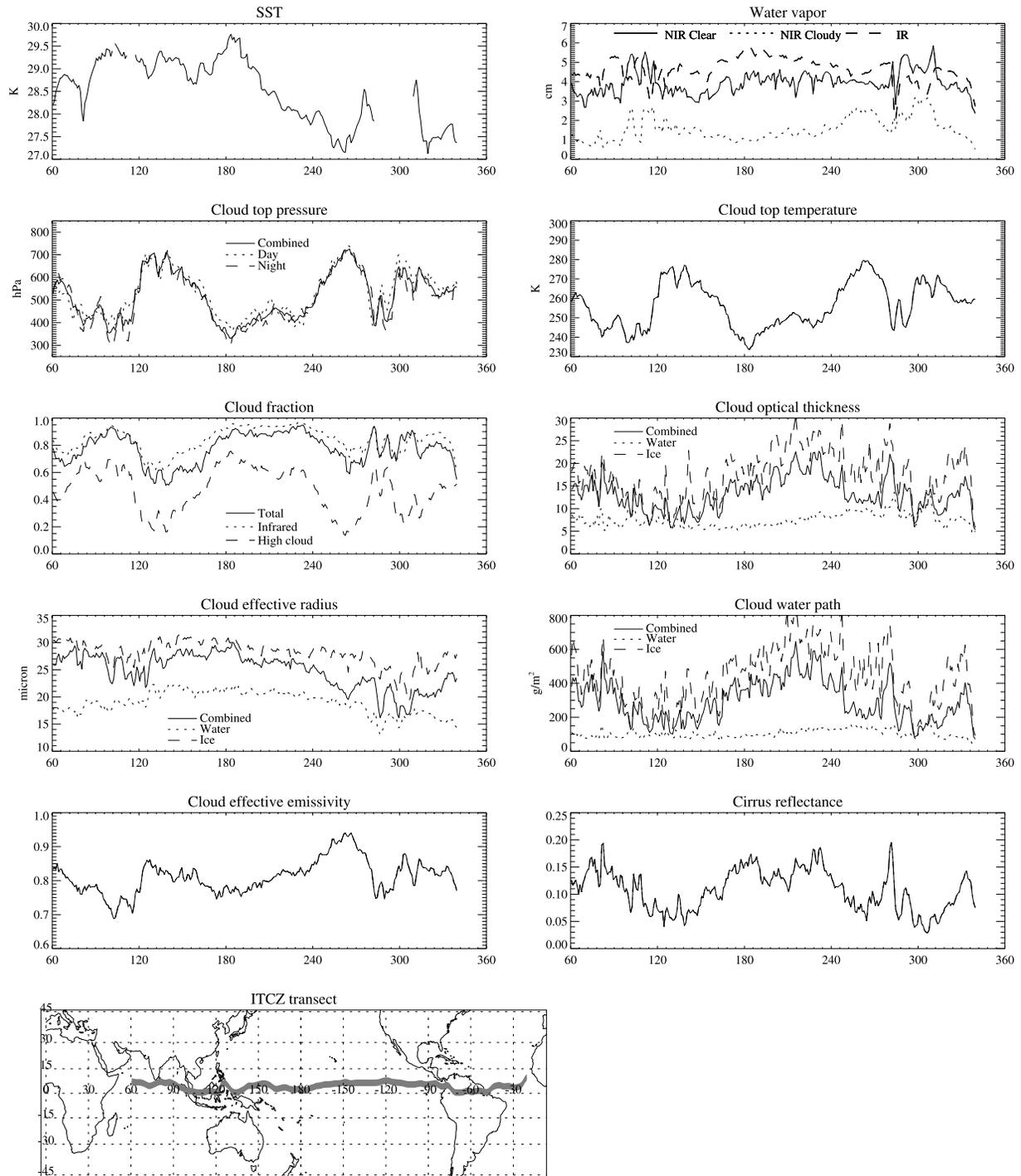
Figure 6. As in Figure 5 but for a transect along the ITCZ, defined at each longitude as the minimum cloud top pressure, except over Africa where the ITCZ is ill-defined. Grid point values are omitted for clarity. Missing values for SST represent land. Abscissa is longitude.

than water cloud radii, but share the tendency for larger radii at higher SST. Water clouds in the ITCZ break cleanly at longitudes 126° E and 84°W (just west of the coast of South America) into two populations, one with larger radius for a given SST (Pacific) and one with smaller radius (Atlantic, Indian oceans). The relationship to SST may be understood partly as an indication of the connection between effective radius and the strength of convective updrafts (R. Houze,

personal communication, 2005) combined with the overall tendency for deepest, most vigorous convection to be associated with higher SSTs. The relationship between cloud top temperature and effective radius (see Figures 1a and 1b, and below), though somewhat weaker than the relationship between SST and effective radius, is in the same sense, with higher colder cloud tops in the ITCZ generally associated with larger effective radius. However,

Table 1. Correlations of Fields in the ITCZ[a]

	SST	q_{clr}	q_{cd}	CTP	CTT	FrT	FrIR	Hifr	Taua	Reffa	CWPa	Eeff	Ci-r
SST	100	2	−40	−37	−43	0	−5	34	−18	71	−5	−69	10
q_{clr}	−	100	57	−31	−26	54	42	21	9	−40	−5	−19	−9
q_{cd}	−	−	100	41	46	0	−17	−52	−33	−79	−52	35	−68
CTP	−	−	−	100	99	−75	−75	−98	−51	−39	−52	76	−68
CTT	−	−	−	−	100	−70	−70	−98	−46	−45	−50	79	−69
FrT	−	−	−	−	−	100	91	69	60	−1	51	−36	50
FrIR	−	−	−	−	−	−	100	72	65	16	62	−30	61
Hifr	−	−	−	−	−	−	−	100	52	45	56	−74	73
Taua	−	−	−	−	−	−	−	−	100	24	93	1	80
Reffa	−	−	−	−	−	−	−	−	−	100	47	−36	62
CWPa	−	−	−	−	−	−	−	−	−	−	100	−4	87
Eeff	−	−	−	−	−	−	−	−	−	−	−	100	−26

[a]SST, sea surface temperature; q_{clr}, column water vapor for clear-sky conditions; q_{cd}, column water vapor above cloud; CTP, cloud top pressure; CTT, cloud top temperature; FrT, cloud fraction (total); FrIR, cloud fraction (IR; see text for difference from FrT); Hifr, high cloud fraction; Taua, optical depth for water and ice clouds; Reffa, cloud particle effective radius for water and ice clouds; CWPa, cloud water path for water and ice clouds; Eeff, effective emissivity; Ci-r, cirrus reflectance.

the difference between the Pacific and the other oceans has no obvious explanation and deserves further study.

[44] Other relationships appear when plotted as a scatterplot matrix (Figure 8). Cloud top temperature and sea surface temperature are inversely associated, with high SST and cold cloud observed together as expected (and vice versa), but for SST above about 27.6°C and below about 29.4°C, a wide range of cloud top temperature is observed (Figure 8d). Conversely, warm cloud tops may be found over a wide range of sea surface temperatures (Figure 8a).

[45] Smallest cloud particles appear over land and hence are not represented in the scatterplot with SST, and effective radius is not a good indicator of cloud top temperature (Figures 8b and 8e), though the converse is not true; warmer cloud tops tend to have somewhat smaller effective radius (Figure 8h).

[46] In the ITCZ, precipitable water shows a fairly strong relationship with SST and also (inversely) with cloud top temperature, slightly less so with precipitable water (fourth row). Plotting any of these quantities against precipitable water (Figures 8j–8l) results in considerably more scatter except for high values (>5 cm) of precipitable water. The driest locations are found over land (compare Figures 8c and 8f).

## 4. Seasonal and Interannual Variability

[47] In order to succinctly characterize the variability of these various fields over the period of record (approximately 5 years in the case of MODIS), we use monthly mean fields and calculate empirical orthogonal functions (EOFs) using spatially smoothed (4° × 4°) data to reduce the size of the matrix that must be inverted. EOFs [e.g., *Pearson*, 1902; *von Storch and Zwiers*, 1999] identify the leading spatial patterns of variability in a data set and the principal components time series (PCs) describe the time dependence of these patterns. Significance of EOFs are evaluated using North's rule of thumb, viz., when the sampling error of the eigenvalues exceeds the separation of neighboring eigenvalues, which is proportional to $1/\sqrt{N}$ [*von Storch and Zwiers*, 1999]. With the large N (1080) used here, all the EOFs shown in Figures 9 and 10 pass North's rule of thumb for significance. We calculated EOFs for April 2000 through December 2004 for a total of six fields, cloud top

temperature, cloud effective radius, cirrus fraction, optical thickness of ice clouds, and both IR and near-IR clear-sky water vapor. Owing to a processing change in October 2003, which affected the mean value of IR water vapor, we have subtracted the means for each grid point before and after the processing change before computing EOFs.

[48] The four leading EOFs of cloud top temperature (Figure 9) describe the seasonal cycle including semiannual harmonics (Figures 9a, 9b, and 9d), as well as interannual variability associated with El Niño–Southern Oscillation (ENSO) (Figure 9c). The first pattern, responsible for 46% of the variance, identifies regions where convection is vigorous during local summer: in the northern hemisphere,
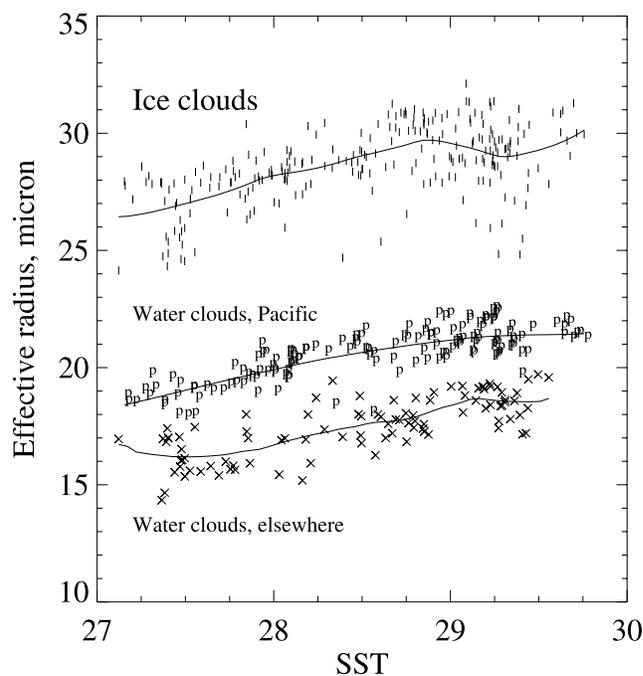
Figure 7. Scatterplot of cloud effective radius against sea surface temperature (°C) along the ITCZ transect shown in Figure 6, for ice clouds and for water clouds over the Pacific "P" and Atlantic/Indian/South American regions, crosses. Smooth curves are calculated using the loess approach [*Cleveland*, 1993].
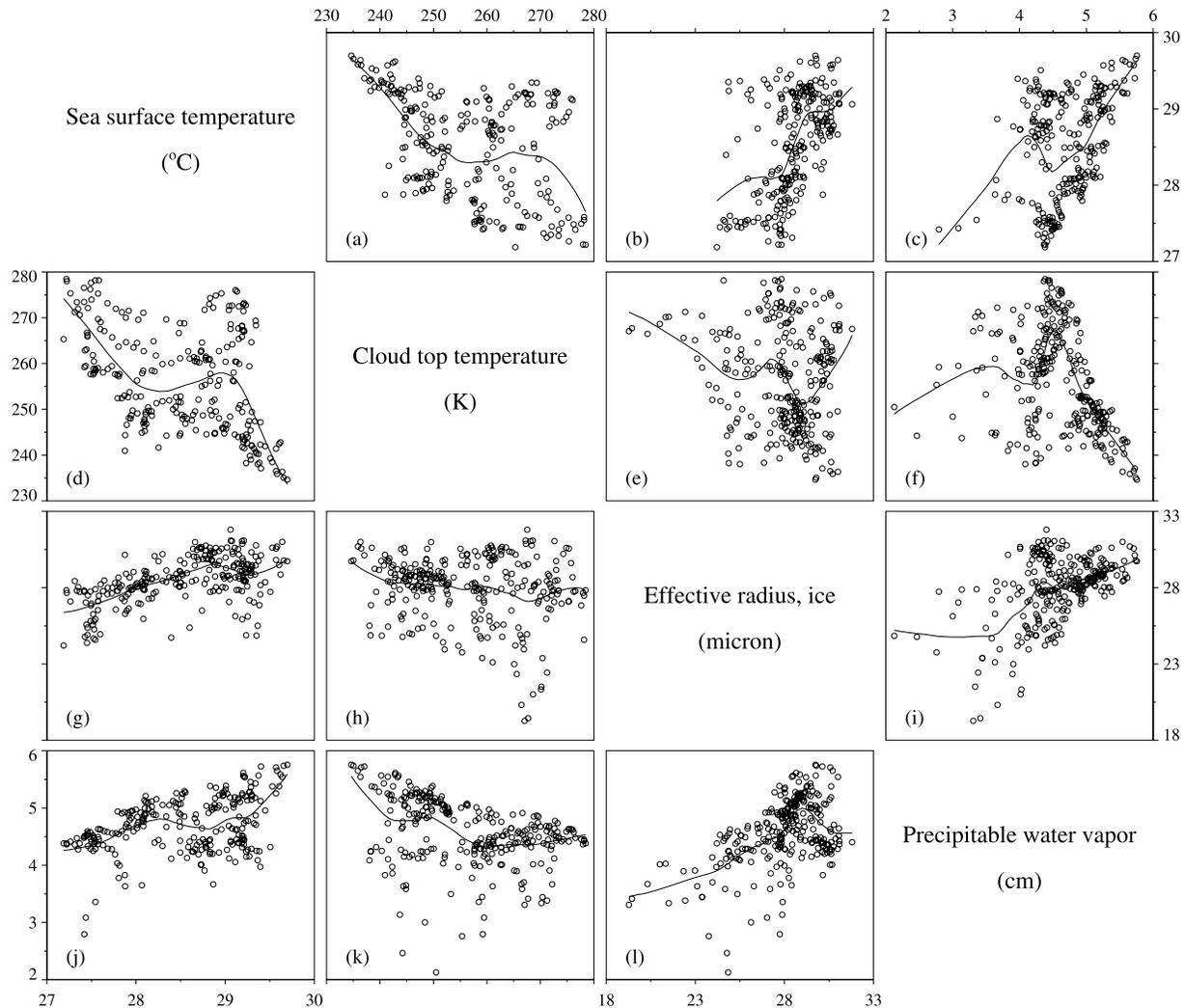
Figure 8. Scatterplots (along the ITCZ transect shown in Figure 6) of the four variables shown, each against the other three. Figures 8a, 8b, 8c, 8e, 8f and 8i and Figures 8d, 8g, 8h 8j, 8k, and 8l show the same pair of variables; loess curves are added using the variable on the abscissa as the dependent variable. Note that some variables have smaller range when plotted against SST, since land points are excluded.

southeast Asia and central America; in the southern hemisphere, southern Africa, central South America, and the "maritime continent" north of Australia. This pattern reaches its maximum amplitude in February and August and has a smooth annual cycle. The second and fourth patterns represent refinements of the annual cycle, especially the transition from northern hemisphere convection to southern hemisphere convection that takes place in October and November, when both modes have maximum amplitude.

[49] Interannual variability associated with El Niño appears as the third EOF, representing a shift in convection from its usual position over the maritime continent toward the central Pacific. By good fortune, there was a moderate El Niño event in 2002–2003 which appears as high values of PC3 then. Interannual variability also appears in the other PCs.

[50] For other fields with spatial patterns that are very similar to those of cloud top temperature (Figure 1), the EOFs and PCs are also very similar. That is, the dominant pattern of

spatial variability represented by cloud top temperature is also the dominant pattern of temporal variability.

[51] The EOFs of IR water vapor, however, are quite different (Figure 10). (The first EOF closely resembles the first EOFs of near-IR clear-sky water vapor in spatial pattern, temporal evolution, and eigenvalue spectrum, despite the differences remarked earlier between the two fields.) The leading pattern, which is much more zonally symmetric than that of cloud top temperature, explains a much larger share (62%) of the variance and represents a strong, smooth annual cycle (Figure 10e) just as for cloud top temperature. The seasonal coherence is one of only a few points of similarity between the leading patterns of the two fields. The next EOF (Figure 10b) describes the semiannual component of the annual cycle, with peaks near the equator that are somewhat larger over oceans than over land. This is essentially the pattern that prevails near the solstices when the amplitude of PC1 is small. The principal component time series associated with this EOF (Figure 10f)
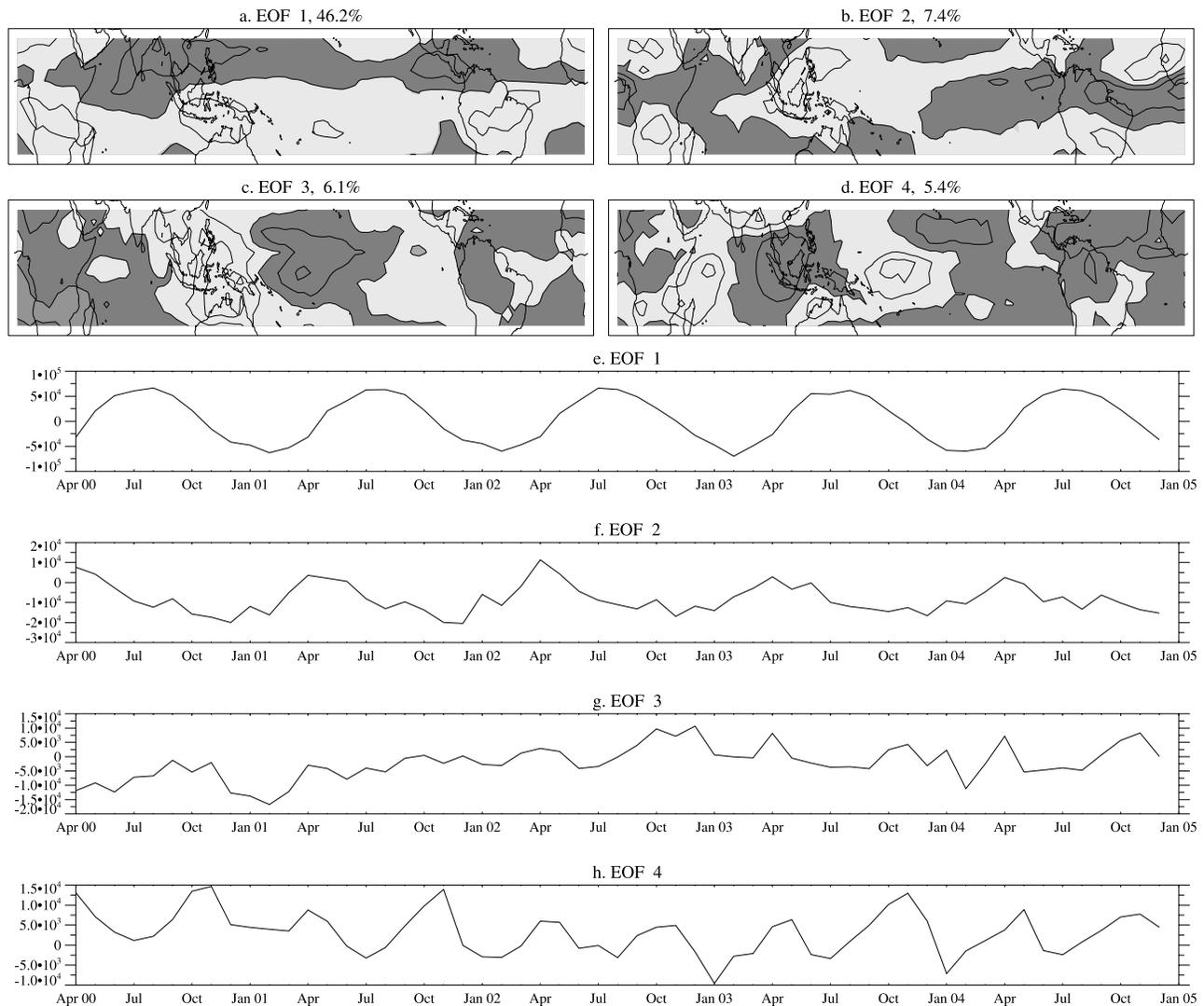
Figure 9. First four empirical orthogonal functions (EOFs) of monthly cloud top temperature from MODIS, for April 2000 to December 2004, and their principal component time series.

has peak amplitude in April and October. The third EOF (Figure 10c) has largest amplitude over the equatorial Pacific and a dominantly annual cycle (Figure 10g). In other words, the first three EOFs describe the mean annual cycle; only the fourth EOF describes ENSO variability, with oppositely signed modes over the Maritime Continent and the central Pacific but with variability on a range of time-scales from seasonal to interannual (Figure 10h).

[52] These results may be contrasted with those of *Bates et al.* [1996], who focused on interannual variations in sea surface temperature, outgoing longwave radiation (OLR), and upper tropospheric water vapor. The leading PCs of each of these fields were highly correlated (>0.8) and although there was a general tendency for high water vapor and low OLR over warm water, the spatial patterns of the leading modes were rather different.

5. Conclusions and Discussion

[53] Most of the cloud and moisture fields observed by MODIS exhibit similar variability in space and time, and are similar to cloud top temperature which can be considered a benchmark field. However, even for highly correlated fields there are also important variations from a simple linear relationship. Some of the ones mentioned in this paper include (1) a close (inverse) correspondence between cloud fraction and cloud top pressure and temperature, except over the eastern subtropical Atlantic and Pacific oceans where strato-cumulus clouds predominate (Figure 1), (2) a distinction between fields with fairly smooth spatial variations (e.g., cloud top pressure, cloud top temperature, cloud fraction, cloud effective emissivity, cloud effective radius, and precipitable water) and those with sharp gradients even in the monthly mean, like cirrus reflectance and cloud optical thickness (Figure 1), (3) sharp topography-related features north of the Himalayas and over the Andes even in the fairly smooth fields, e.g., precipitable water over the Andes and cloud top pressure north of the Himalayas (Figure 1), (4) strong dependence of precipitable water on sea surface temperature, except in the eastern tropical Atlantic and Pacific (Figure 2), (5) as in previous studies, the existence of an upper tropospheric mode in cloud top height (or pressure or temperature) (Figure 3), (6)
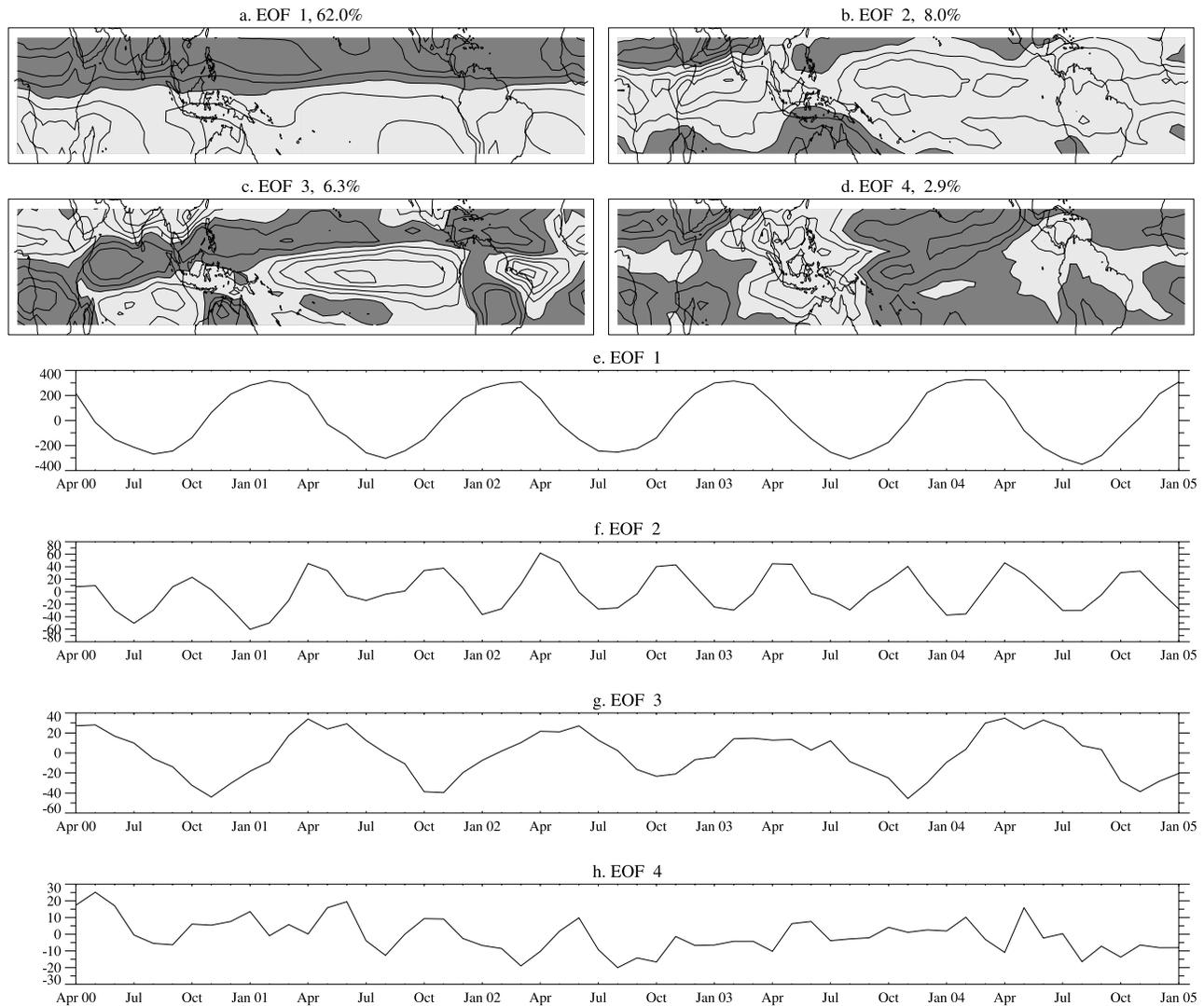
Figure 10.   As in Figure 9 but for IR clear-sky water vapor.

strong tendencies for optically thin clouds to have high cloud top temperature, for optically thick clouds to have low cloud top temperature, and for all but the coldest clouds to have low optical thickness (Figure 4), (7) distinctly different properties in the subsiding regions of the northern and southern subtropics in the eastern Pacific (Figure 5), (8) dependence of effective radius on sea surface temperature for both ice clouds and water clouds, that is (in the case of water clouds) different for the Pacific Basin and the other two ocean basins (Figure 7), (9) over the life of Terra, with spatiotemporal variability in cloud top temperature dominated by the seasonal cycle (over 50% of the variance in the first two EOFs) whose variability is dominated by the NH and SH features over southeast Asia/ Bay of Bengal and central America/eastern Pacific in one season (peaking in August) and maritime continent/tropical south America in the other season (peaking in February); ENSO variability shows up in the third EOF with only 6% of the variance (Figure 9), and (10) the strong seasonal cycle in column water vapor (76% of the variance) is rather different from the seasonal cycle in cloud top temperature. ENSO variability is weakly present in the fourth EOF (3% of the variance) (Figure 10).

[54]   Clear-sky water vapor exhibits variability in space and time that is almost completely distinct from that of the collection of other fields. It exhibits less sensitivity to geographical controls like the continental convective areas and locations of high sea surface temperature, except in the southern subtropics, and it also exhibits less sensitivity to ENSO. This stands in contrast to several other studies [e.g., *Bates et al.*, 1996; *Liao and Rind*, 1997; *Chen et al.*, 1999; *Mote et al.*, 2000] that have identified a close relationship between upper tropospheric water vapor and convection on intraseasonal, seasonal, and interannual timescales. To be sure, convection moistens the upper troposphere (except perhaps at altitudes above about 150 hPa), but column-integrated water vapor appears to respond to a different drummer. Given its importance as the planet's dominant greenhouse gas, this variability needs to be better understood. The large suite of observations provided by MODIS and other instruments aboard the Terra and Aqua satellites are a valuable trove of data for such studies.

[55]   The sheer size of this trove, however, poses challenges. A number of available data products have problems, some of which are documented, some of which could be

elicited only after personal contact with the instrument teams. Possibly spurious land-sea contrasts in cloud top pressure and precipitable water (Figures 1b and 1j), for example, are not well understood and may be a retrieval problem. Extensive examination of all of these products is needed, both to compare fields with each other and to compare the new MODIS products with other observations as has been done in some published studies.

References

Barnes, W. L., T. S. Pagano, and V. V. Salomonson (1998), Prelaunch characteristics of the Moderate Resolution Imaging Spectroradiometer (MODIS) on EOS-AM1, *IEEE Trans. Geosci. Remote Sens.*, *36*, 1088–1100.

Bates, J. J., X. Wu, and D. L. Jackson (1996), Interannual variability of upper-tropospheric water vapor band brightness temperature, *J. Clim.*, *9*, 427–438.

Brown, R. G., and C. Zhang (1997), Variability of mid-tropospheric humidity and its effect on cloud-top height distribution during TOGA COARE, *J. Atmos. Sci.*, *54*, 2760–2774.

Chen, M., R. B. Rood, and W. G. Read (1999), Seasonal variations of upper tropospheric water vapor and high clouds observed from satellites, *J. Geophys. Res.*, *104*, 6193–6197.

Cleveland, W. S. (1993), *Visualizing Data*, 360 pp., Hobart, Summit, N. J.

Frey, R. A., S. A. Ackerman, and B. J. Soden (1996), Climate parameters from satellite spectral measurements. Part 1: Collocated AVHRR and HIRS/2 observations of spectral greenhouse parameter, *J. Clim.*, *9*, 327–344.

Gao, B.-C., and Y. J. Kaufman (2003), Water vapor retrievals using Moderate Resolution Imaging Spectroradiometer (MODIS) near-infrared channels, *J. Geophys. Res.*, *108*(D13), 4389, doi:10.1029/2002JD003023.

Gao, B.-C., P. Yang, W. Han, R.-R. Li, and W. J. Wiscombe (2002), An algorithm using visible and 1.38-micron channels to retrieve cirrus cloud reflectances from aircraft and satellite data, *IEEE Transactions on Geoscience and Remote Sensing*, *40*, 1659–1668.

Gao, B.-C., P. Yang, G. Guo, S. K. Park, W. J. Wiscombe, and B. Chen (2003), Measurements of water vapor and high clouds over the Tibetan plateau with the Terra MODIS instrument, *IEEE Transactions on Geoscience and Remote Sensing*, *41*, 895–900, doi:10.1109/TGRS.2003.810704.

Hartmann, D. L., L. A. Moy, and Q. Fu (2001), Tropical convection and the energy balance at the top of the atmosphere, *J. Clim.*, *14*, 4495–4511.

Heymsfield, A., S. Matrosov, and B. Baum (2003), Ice water path-optical depth relationships for cirrus and deep stratiform ice cloud layers, *J. Appl. Meteorol.*, *42*, 1369–1390.

Hollars, S., Q. Fu, J. Comstock, and T. Ackerman (2004), Comparison of cloud-top height retrievals from ground-based 35 GHz MMCR and GMS-5 satellite observations at ARM TWP Manus site, *Atmos. Res.*, *72*, 169–186.

Johnson, R. H., R. M. Rickenbach, S. A. Rutledge, P. E. Ciesielski, and W. H. Schubert (1998), Trimodal characteristics of tropical convection, *J. Clim.*, *12*, 2397–2418.

King, M. D., W. P. Menzel, Y. J. Kaufman, D. Tanré, B.-C. Gao, S. Platnick, S. A. Ackerman, L. A. Remer, R. Pincus, and P. A. Hubanks (2003), Cloud and aerosol properties, precipitable water, and profiles of temperature and

water vapor from MODIS, *IEEE Trans. Geosci. Remote Sens.*, *41*, 442–458, doi:10.1109/TGRS.2002.808226.

Larson, K., and D. L. Hartmann (2003a), Interactions among cloud, water vapor, radiation, and large-scale circulation in the tropical climate. Part I: Sensitivity to uniform sea surface temperature changes, *J. Clim.*, *16*, 1425–1440.

Larson, K., and D. L. Hartmann (2003b), Interactions among cloud, water vapor, radiation, and large-scale circulation in the tropical climate. part II: Sensitivity to spatial gradients of sea surface temperature, *J. Clim.*, *16*, 1441–1455.

Lau, K.-M., C.-H. Ho, and M.-D. Chou (1996), Water vapor and cloud feedback over the tropical oceans: Can we use ENSO as a surrogate for climate change?, *Geophys. Res. Lett.*, *21*, 2971–2974.

Liao, X., and D. Rind (1997), Local upper tropospheric/lower stratospheric clear-sky water vapor and tropospheric deep convection, *J. Geophys. Res.*, *102*, 19,543–19,557.

McGarry, M. M., and R. J. Reed (1978), Diurnal variations in convective cloud activity and precipitation during phases II and III of GATE, *Mon. Weather Rev.*, *106*, 101–113.

Mote, P. W., H. L. Clark, T. J. Dunkerton, R. S. Harwood, and H. C. Pumphrey (2000), Intraseasonal variations of water vapor in the tropical upper troposphere and tropopause region, *J. Geophys. Res.*, *105*, 17,457–17,470.

Pearson, K. (1902), On lines and planes of closest fit to systems of points in space, *Philos. Mag.*, *2*, 559–572.

Platnick, S., M. D. King, S. A. Ackerman, W. P. Menzel, B. A. Baum, J. C. Riédi, and R. A. Frey (2003), The MODIS cloud products: Algorithms and examples from Terra, *IEEE Trans. Geosci. Remote Sens.*, *41*, 459–473, doi:10.1109/TGRS.2002.808301.

Reynolds, R. W., N. A. Rayner, T. M. Smith, D. C. Stokes, and W. Wang (2002), An improved in situ and satellite SST analysis for climate, *J. Clim.*, *15*, 1609–1625.

Seemann, S. W., J. Li, W. P. Menzel, and L. E. Gumley (2003), Operational retrieval of atmospheric temperature, moisture, and ozone from MODIS infrared radiances, *J. Appl. Meteorol.*, *42*, 1072–1091.

Sherwood, S. C. (2002), Aerosols and ice particle size in tropical cumulonimbus, *J. Clim.*, *15*, 1051–1063.

Soden, B. J. (2004), The impact of tropical convection and cirrus on upper tropospheric humidity: A Lagrangian analysis of satellite measurements, *Geophys. Res. Lett.*, *31*, L20104, doi:10.1029/2004GL020980.

Stephens, G. L. (2005), Cloud feedbacks in the climate system: A critical review, *J. Clim.*, *18*, 237–273.

Stephens, G. L., et al. (2002), The Cloudsat mission and the A-Train, *Bull. Am. Meteorol. Soc.*, *83*, 1771, doi:10.1175/BAMS-83-12-1771.

Tian, B., B. J. Soden, and X. Wu (2004), Diurnal cycle of convection, clouds, and water vapor in the tropical upper troposphere: Satellites versus a general circulation model, *J. Geophys. Res.*, *109*, D10101, doi:10.1029/2003JD004117.

von Storch, H. V., and F. W. Zwiers (1999), *Statistical Analysis in Climate Research*, 484 pp., Cambridge Univ. Press, New York.

Wang, P.-H., M. P. McCormick, P. Minnis, G. S. Kent, G. K. Yue, and K. M. Skeens (1995), A method for estimating vertical distribution of the SAGE II opaque cloud frequency, *J. Geophys. Res.*, *22*, 243–246.

Wheeler, M. C., and H. H. Hendon (2004), An all-season real-time multivariate MJO index: Development of an index for monitoring and prediction, *Mon. Weather Rev.*, *132*, 1917–1932.

Wylie, D. P., and P.-H. Wang (1997), Comparison of cloud frequency data from the high-resolution infrared radiometer sounder and the Stratospheric Aerosol and Gas Experiment II, *J. Geophys. Res.*, *102*, 29,893–29,900.

Zhang, C., B. E. Mapes, and B. J. Soden (2003), Bimodality in tropical water vapor, *Q. J. R. Meteorol. Soc.*, *129*, 2847–2866.

———————————

R. Frey, Space Science and Engineering Center, University of Wisconsin, 1225 West Dayton Street, Madison, WI 53706, USA.

P. W. Mote, NorthWest Research Associates, P.O. Box 3027, Bellevue, WA 98009, USA. (mote@nwra.com)